ELSEVIER

Contents lists available at ScienceDirect

Materials Science & Engineering A

journal homepage: http://www.elsevier.com/locate/msea





Thermomechanically influenced dynamic elastic constants of laser powder bed fusion additively manufactured Ti6Al4V

Mangesh V. Pantawane ^{a,c}, Teng Yang ^{b,c}, Yuqi Jin ^b, Sangram Mazumder ^{a,c}, Mayur Pole ^a, Sriswaroop Dasari ^a, Arkadii Krokhin ^b, Arup Neogi ^{b,c}, Sundeep Mukherjee ^a, Rajarshi Banerjee ^{a,c}, Narendra B. Dahotre ^{a,c,*}

- ^a Department of Materials Science and Engineering, University of North Texas, Denton, TX, 76207, USA
- b Department of Physics, University of North Texas, Denton, TX, 76203, USA
- ^c Center for Agile and Adaptive Additive Manufacturing, University of North Texas, Denton, TX, 76207, USA

ARTICLE INFO

Keywords: Elastic constants Thermal stress Additive manufacturing Ultrasound technique

ABSTRACT

This paper reports the dynamic elastic constants of laser powder bed fusion additively manufactured Ti6Al4V alloy by recently developed effective bulk modulus elastography technique and compares them with the static elastic constants evaluated using the nanoindentation technique. With this elastography technique, two ultrasound frequencies (10 MHz and 20 MHz) were employed, which distinctly identified spatially varying the dynamic elastic constants and effective density in additively manufactured Ti6Al4V while comparing to the wrought Ti6Al4V. The spatial resolution of elastic constants and effective density of the scanned region significantly improved at 20 MHz ultrasound frequency. The dynamic elastic constants were 5%–8% lower than static elastic constants obtained for the additively manufactured Ti6Al4V and wrought Ti6Al4V. In addition, the present study compares the elastic moduli of additively manufactured Ti6Al4V, wrought Ti6Al4V, and solutionized and water quenched wrought Ti6Al4V. The microstructural examination of additively manufactured Ti6Al4V using scanning electron microscopy revealed a high density of internal twins within martensite laths contrary to scarcely twinned martensite lath in water quenched wrought Ti6Al4V. The origin of such high defect density was realized by a thermo-mechanical computational model that predicted rapidly changing alternating tensile-compressive stresses in the range of 49–720 MPa that, in turn, affected the dynamic and static elastic constants.

1. Introduction

The additive manufacturing (AM) approach carries a key benefit of material efficiency besides various other features, including but not limited to intricate design, cost efficiency, and surface finish [1,2]. While the material loss has significantly been brought down through AM, the bulk mechanical properties of AM materials are still being widely characterized through destructive techniques. The static mechanical properties of the material are used as a standard for presenting the fundamental properties of the material. The conventional techniques for evaluation of the static properties of material using machining, polishing or indentation can modify the intrinsic structure developed during the AM process [3]. Metal cutting or machining is normally carried out at a high speed that can result in the generation of heat due to

friction [4] and generation of adiabatic shear locally. Some of these properties (creep and fracture toughness) are impractical to inspect using non-destructive testing (NDT) due to principal reasons. Although few mechanical testings have been evolved through quasi-non-destructive measurements and testings of miniaturized components, they remain confined by the experimental limitations [5]. Furthermore, the static tests are not reliable in a variety of applications where the material experiences rapidly-changing and dynamic loading conditions as in case of Ti6Al4V, which is an alloy of Titanium widely used in aerospace and defense owing to its excellent set of structural properties

Elastic constants of metallic alloys are estimated under static conditions using standard destructive tests. These elastic constants are of paramount importance considering engineering design, applications,

^{*} Corresponding author. Department of Materials Science and Engineering, University of North Texas, Denton, TX, 76207, USA. *E-mail address:* narendra.dahotre@unt.edu (N.B. Dahotre).

and to describe their mechanical behavior. They are intrinsic to material and stem from interatomic separation and bond energy [6]. This fundamental nature is subject to change considerably with the manufacturing technique. Especially, the laser-based AM techniques such as laser powder bed fusion (LPBF) and direct energy deposition (DED), due to their rapid and distinct thermokinetics, yield near non-equilibrium lattice structures [7,8]. Besides this change in the thermodynamic state, the rapid and repetitive thermokinetics inherent to the laser-based AM process can significantly affect the intrinsic mechanical nature of the material.

Measurement of elastic moduli using a conventional/standard static tests requires sample in specific dimensions and multiple tests with large strains and low strain rates in the elastic regime. On the other hand, the dynamic tests non-destructively provide a comparatively accurate estimation of elastic properties and are carried under a rapid strain rate with a significantly low strain (few microstrains). Ultrasound techniques, aside from detecting three-dimensional volume defects (pores, cracks, and inclusion) in the material, can determine the dynamic elastic properties with sound wave exposure in longitudinal and transverse mode [9]. These techniques are continuously evolving to newer dimensions. Recently, the Effective Bulk Modulus Elastography (EBME) was developed using monostatic longitudinal ultrasonic pulsing without external stress [10,11]. The technique determines the elastic properties of the material at the exposed ultrasound frequency.

The AM approach offers equally important processing versatility in addition to the flexibility of varying alloy constituents to rapidly develop newer material with a unique set of characteristics. However, the conventional static tests to determine their elastic constants through many trials to standardize them is laborious and undesirable for materials employed under dynamic conditions. In view of this, the primary objective of the current study is to report the potential of the newly developed EBME technique to detect the spatially varying dynamic elastic constants of Ti6Al4V additively manufactured using laser powder bed fusion (LPBF-AM). The dynamic elastic constants using the EBME technique are then compared with the static elastic constants obtained using the nanoindentation technique. In parallel, these tests were also performed on the conventionally manufactured and annealed form of wrought Ti6Al4V. Another objective of the present study is to recognize the effect of processing techniques (LPBF-AM and conventional solutionizing-water-quenched treatment) on the thermodynamic state of the resultant phases and, in turn, on the elastic constants. This objective was met by comparing the static elastic moduli of LPBF-AM Ti6Al4V and wrought Ti6Al4V solutionized and quenched in water (WQ-Ti6Al4V). Furthermore, the effect of non-equilibrium phases and process-inherent

complex thermokinetic and thermo-mechanical nature on the elastic constants of the LPBF-AM Ti6Al4V were recognized through a multiphysics computational model based on the finite element method (FEM).

2. Materials and methods

2.1. Fabrication

Ti6Al4V blocks of 1.5 cubic inch (38.1mm \times 38.1mm \times 38.1 mm) were printed in AconityMIDI using LPBF-AM technique with grade-23 powder particles ranging 15–45 µm. The operating parameters of CW Nd:YAG ($\lambda=1070$ nm) laser of 85 µm beam diameter included 150 W power, 800 mm/s scanning speed, and 30 µm layer thickness. Each layer fabrication involved bi-directional laser scanning, where consecutive linear laser tracks were inversely directed and separated by 120 µm between their centers. Scanning orientation in each layer was rotated by 90° after an interlayer delay of 16s. The activity of oxygen in the processing chamber was kept below 50 ppm. The input energy density as per the involved laser and process parameters was 52.08 J/mm³. The image of LPBF-AM block of Ti6Al4V depicting build direction (Z) and the laser scanning strategy is provided in Fig. 1.

The printed components were analyzed for their microstructure using nano scanning electron microscope (SEM) by FEI. Accurate measurement of density of wrought and LPBF-AM Ti6Al4V was carried out using pycnometer with nitrogen gas. The test was repeated multiple times on different regions of the wrought and LPBF-AM Ti6Al4V. In addition to the LPBF-AM Ti6Al4V and wrought Ti6Al4V, the tests were also performed on the conventionally heat-treated 1 mm³ block of wrought Ti6Al4V, which involved solutionizing at 1323 K for 15 min followed by quenching in water. This treatment was done explicitly on 1 mm³ volume of wrought Ti6Al4V to obtain an uniformly high cooling rate (>410 K/s) throughout the entire volume in order to achieve the formation of the martensite phase in the volume [12].

2.2. Numerical modeling

In view of the limitations of existing thermal sensing techniques to probe the transient temperature distribution during dynamic LPBF-AM fabrication, a multiphysics thermal model was developed using finite element method on the COMSOL multiphysics platform. First component of the numerical model predicted the transient temporal temperature distribution associated with the complex thermokinetics involving repetitive and rapid heating-cooling, and fluctuating steep thermal gradients during LPBF-AM fabrication. Such complex thermokinetics

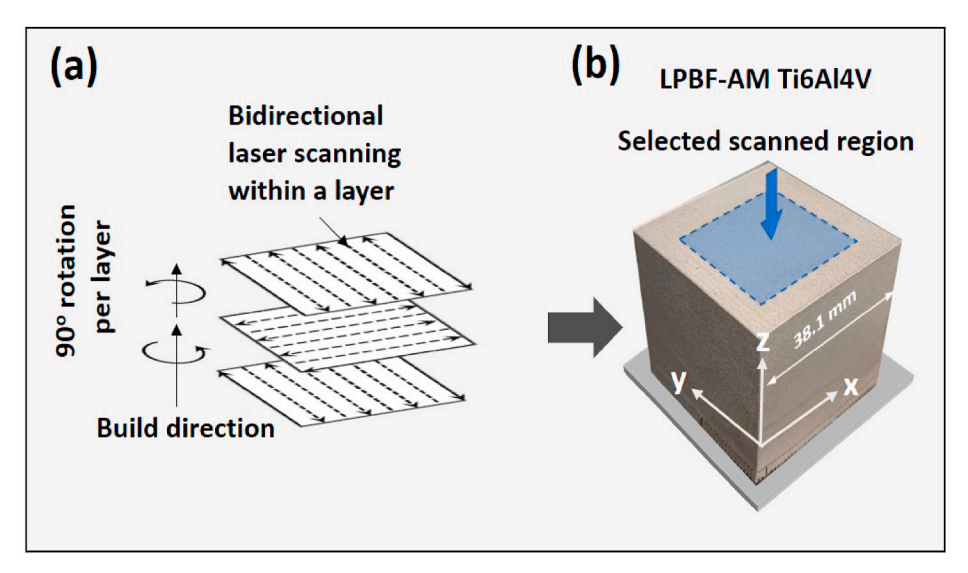


Fig. 1. The image of LPBF-AM Ti6Al4V block with assigned direction and dimensions.

leads to evolution of complex thermomechanical state in the material. Hence, the transient temperature field computed via first component of the numerical model was coupled in the second component on structural mechanics of the model to predict evolution of complex state of stress and strain which eventually affected the physical properties of the LPBF processed material. The theoretical development of the thermokinetic model detailing governing equations, boundary conditions, and assumptions are adopted from the recent reports of the authors [7,8].

For computation of thermo-mechanical stress evolution, the transient temperature field computed via thermal model was coupled with structural mechanics model for thermal strain (ϵ^{th}) evaluation using following Eq. 1

$$d\varepsilon^{th} = \alpha_T \Delta T \tag{1}$$

where, α_T is the coefficient of thermal expansion and ΔT considers the change in reference temperature with respect to temperature field.

The total strain increment primarily consists of increments due to elastic (de^{el}) , plastic (de^{pl}) and thermal (de^{th}) strain components. The plastic strain (de^{pl}) is influenced by the yield function (F_y) , stress (σ) , and hardening parameter (λ) as follows-

$$d\varepsilon^{pl} = d\lambda \left(\frac{\partial F_{y}}{\partial \sigma}\right) \tag{2}$$

The yield function was considered based on the von Mises yield criterion as per Eq. 3

$$F_{y} = \sigma_{von} - \sigma_{ys} \left(\varepsilon_{eff(pl)} \right) \tag{3}$$

where σ_{von} is von Mises stress and $\sigma_{ys}(\varepsilon_{eff(pl)})$ is yield stress as a function of effective plastic strain. Eventually using isotropic hardening modulus (E_{iso}) , the yield stress can be related to the initial yield stress (σ_{ys0}) and $\varepsilon_{eff(pl)}$ using Eq. (4).

$$\sigma_{vs}(\varepsilon_{eff(pl)}) = \sigma_{vs0} + E_{iso}\varepsilon_{eff(pl)} \tag{4}$$

The isotropic hardening modulus was obtained using tangent modulus. Additional mechanical properties of Ti6Al4V alloy were referred from the recent literature [13].

2.3. Ultrasound technique

The given regions of the LPBF-AM and wrought Ti6Al4V block were scanned using Olympus Panametrics V211 0.125-inch diameter (shear wave) and V312 0.125-inch diameter (longitudinal wave) unfocused immersion transducers at 10 MHz and 20 MHz. The unfocussed immersion transducers with a low (10 MHz) and a high (20 MHz) frequency were used in order to identify their effect on the spatial resolution due to change in the frequency. The former transducer recorded the shear wave velocity at several spots on the sample at different rotations along the axis perpendicular to scanned surface (Fig. 1). The latter transducer was used to generate pulses for the raster scans of samples, and record signals reflected by the sample (Fig. 1). A JSR Ultrasonic DPR 300Pulse/Receiver internally operated the pulse source and time trigger and the data was collected by a Tektronix MDO 3024b. The scanning rate was maintained at 512 signals per 20s. Here, it should also be noted that 0.125-inch (3.175 mm) diameter of both Olympus Panametrics V211 (shear wave) and V312 (longitudinal wave) immersion transducers employed for EBME measurements in the present study restricted EBME scanning measurements to not less than the length scale of 0.125-inch (3.175 mm). Hence, the WQ-Ti6Al4V (1 mm³ blocks) were not characterized using EBME technique.

Based on the recently developed EMBE technique [10,11], the effective density ρ and dynamic bulk modulus K_d mapping are calculated by measuring the acoustic impedance of scanned sample using the classical speed of sound theory: $K_d = Zc$ and $\rho = Z/c$, where Z is the acoustic impedance of the sample, ρ is the effective density, and c is the

velocity of sound in sample. EBME technique used deionized water as an ambient fluid due to its stable and known properties as reference values to calculate Z. The reverse behavior of temperature dependent material density and speed of sound provides minimal or no variation with minor variation of the ambient temperature in the acoustic impedance of the reference deionized water. During the experiment, the transducer emitted pulse envelope is separated into two echoes at the front and back interfaces of the sample material surrounded by water environment due to an impedance contrast between the sample material and the reference ambient fluid. Comparing the pre-calibrated pressure value with the emission source, the sample acoustic impedance (Z_1) can be calculated by the known acoustic impedance (Z_0) of deionized water and the ratio of the second echo and the difference between the emitted wave with the first echo as given in Eq. 5

$$\frac{Z_1}{Z_0} = \frac{-1 - \alpha - \sqrt{4\alpha + 1}}{\alpha - 2} \tag{5}$$

where $\alpha = \frac{P_1}{P_e - sign(Z_1 - Z_0)|P_0|}$ is the experimental factor calculated using p_e , which is the sound pressure of the emission source, and P_0 and P_1 which are experimentally measured sound pressure of the first and second reflection from the front and rear surface of the block.

With the temporal delay of the two reflected envelopes, the longitudinal speed of sound (G_L) can be determined in the material. This allows calculating K_d and ρ using Eqs. (6) and (7), respectively.

$$K_d = C_L Z_0 \frac{-1 - \alpha - \sqrt{4\alpha + 1}}{\alpha - 2} \tag{6}$$

$$\rho = \frac{Z_0}{C_L} \frac{-1 - \alpha - \sqrt{4\alpha + 1}}{\alpha - 2} \tag{7}$$

Effective dynamic shear modulus (G_d) can be calculated using following Eq. (8), where C_T is the speed of the transverse wave. With this data, the effective dynamic Young's modulus (E_d) and Poisson's ratio (ν_d) can be calculated using Eqs. (9) and (10).

$$G_d = \rho C_T^2 \tag{8}$$

$$E_d = \frac{9K_dG_d}{3K_d - G_d} \tag{9}$$

$$\nu_d = \frac{3K_d - 2G_d}{2(3K_d - G_d)} \tag{10}$$

It should be noted that, in addition to dynamic modulus, Eqs. (9) and (10) in their standard form are pertinent to determine the static moduli of the material.

2.4. Nanoindentation

To compare the dynamic elastic modulus obtained using EBME technique, the elastic modulus was obtained in static condition using nano-indentation test. This test involved nano-identation on LPBF-AM, wrought Ti6Al4V, and WQ-Ti6Al4V, using TI-premier Triboindenter (Broker, Minneapolis, MN, USA) with a diamond Berkovich tip at ambient temperature. A load was gradually increased up to 1 N in 5s and dwelt for 2s and unloading was achieved in 5s. Several indents (16) were made in different regions of both samples to notice a recognizable difference between their load vs. depth behaviors during loading and unloading of testing. By Hertzian theory of contact mechanics, the nano-identation technique provides reduced Youngs modulus (E_r) as per Eq. (11), which is comprised based on deformation of sample and indentor. Thus, the actual Youngs modulus (E_s) of the sample was obtained by Eq. (12).

$$E_r = \frac{\sqrt{\pi}}{2} \frac{S}{\sqrt{A_r}} \tag{11}$$

$$\frac{1}{E_r} = \frac{\left(1 - \nu_s^2\right)}{E_s} + \frac{\left(1 - \nu_i^2\right)}{E_i} \tag{12}$$

where S is the slope of unloading curve at maximum depth and A_c is the contact area of the indentor at the same instant of maximum depth. ν_s and ν_i (0.07) correspond to Poisson's ratio of sample and the indentor, respectively. E_i (1141 GPa) is the Young's modulus of the indentor.

3. Results and discussion

3.1. Characteristics in static condition

The characteristic load versus depth plot of LPBF-AM Ti6Al4V, wrought Ti6Al4V, and WQ-Ti6Al4V obtained by nanoindentation is presented in Fig. 2. Young's moduli and hardness of these samples, based on nanoidentation test, along with other static elastic constants calculated using Eqs. (9) and (10), are listed in Table 1. Here it should be noted that the Poisson's ratio considered while calculating other elastic constants is different for both wrought and LPBF-AM Ti6Al4V. This variation is considered due to the evolution of distinctly different phase/ micro structures within these sample, thereby changing their mechanical characteristics. The wrought Ti6Al4V is usually a mixture of α and β phases while LPBF-AM Ti6Al4V and WQ-Ti6Al4V mostly consists of α' martensitic phase. It can be seen that the static elastic constants values corresponding to LPBF-AM Ti6Al4V are relatively lower than its conventionally fabricated wrought form (22–26%) and higher than that of WQ-Ti6Al4V (18-21%)(Table 1). The hardness values of WQ-Ti6Al4V (4.34±0.05 GPa) were higher compared to that of LPBF-AM Ti6Al4V $(3.63\pm0.07 \text{ GPa})$ and wrought Ti6Al4V $(3.84\pm0.17 \text{ GPa})$.

In density measurement by pycnometer, the LPBF-AM Ti6Al4V marginally (0.16%) exceeded the average density of wrought Ti6Al4V and WQ-Ti6Al4V within the higher sensitivity limits of the pycnometer. This indicates that in spite of the complex fluid dynamics and thermokinetics associated with LBPF-AM process that generally leads to a higher probability of generating three-dimensional physical (morphological) defects (pores and cracks), under the set of LBPF-AM processing parameters employed in the present work and mentioned earlier, no such detectable defects existed in the sample which was also later confirmed by optical and SEM microscopy observations.

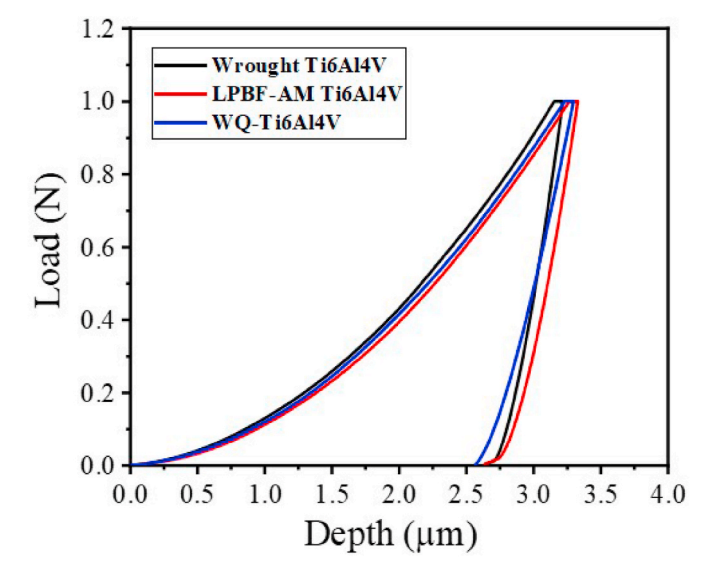


Fig. 2. Load versus indentation depth plot of LPBF-AM Ti6Al4V,wrought Ti6Al4V, and WQ-Ti6Al4V.

Table 1Static elastic constant, hardness, and density of LPBF-AM, wrought Ti6Al4V, and WO-Ti6Al4V.

Properties	LPBF-AM Ti6Al4V	Wrought Ti6Al4V	WQ-Ti6Al4V
Reduced Young's Modulus (E_r/GPa)	133.91±0.79	149.06±3.93	110.04±1.5
Static Young's Modulus (E_s/GPa)	$136.27 {\pm} 0.71$	151.52 ± 3.58	109.80 ± 1.35
Static Bulk Modulus (K_s/GPa)	$124.78 {\pm} 0.65$	157.83 ± 3.72	100.54±0.59
Static Shear Modulus (G_s/GPa)	51.69 ± 0.26	56.53±1.33	41.65±0.21
Static Poisson's Ratio (ν_s)	0.318 [14]	0.34 [15]	0.318 [14]
Hardness (H/GPa)	$3.63{\pm}0.07$	$3.84{\pm}0.17$	$4.34{\pm}0.05$
Density ($\rho/\text{Kg}m^{-3}$)	4475±1.4	$4468{\pm}2.01$	$4476{\pm}2.1$

3.2. Characteristics in dynamic condition

Based on the EBME technique described earlier, LPBF-AM and wrought Ti6Al4V were scanned at 10 MHz and 20 MHz to compute effective dynamic bulk modulus (K_d) and density (ρ). The planar contour plots of the scans in 3D volume from the top face (XY; Fig. 1b) of LPBF-AM block, were generated to reveal an average distinct spatial distribution of K_d and ρ (Fig. 3a–d). The average spatial resolution of both K_d and ρ clearly and significantly increased in the planar contour plots of 20 MHz compared to that of 10 MHz (Fig. 3a-d). This is attributed to lower ultrasound wavelength at higher frequency (20 MHz) which may be influenced by the microstructural aspects such as crystallographic defects present in the material. Furthermore, although overall values of K_d and ρ for 10 MHz were slightly higher than those for 20 MHz, the variation of these values for 10 MHz (K_d :105.9–106.4 GPa; ρ :4385–4405 Kg/m^3) was confined to a narrow range compared to that for 20 MHz $(K_d:101-104.5 \text{ GPa}; \rho:4240-4440 \text{ Kg/}m^3)$ emphasizing the higher spatial resolution associated with measurements at 20 MHz. In addition, with the higher spatial resolution at 20 MHz, relatively uniform K_d and ρ values are noticeable within the core of the scanned region (represented by large contour islands) while relatively non-uniform distribution of K_d and ρ values represented by small contour islands towards the edges of block. This effect is likely to arise due to the bidirectional scanning strategy employed in the current study that is also likely to influence the stress distribution and modulus of LPBF-AM block.

Typically, a heterogeneous microstructure is reported for the samples manufactured via laser-based additive manufacturing techniques [16], which, in turn, generate microscale residual stresses [17]. Such a microscale heterogeneity, in addition to process induced macro spatial thermokinetic variation [7] is likely to lead to macroscale heterogeneity of the stresses, which, in turn, is reflected in spatial variation of K_d and ρ detected at 20 MHz.

From the values of effective density obtained via the EBME technique and the measured shear wave velocity using shear transducer, the shear modulus was derived at various locations of LPBF-AM and wrought Ti6Al4V. Eventually, all the dynamic constants were evaluated using Eqs. (9) and (10) and are listed in Table 2. The lower dynamic elastic constants corresponding to LPBF-AM Ti6Al4V than those of wrought Ti6Al4V follows the similar comparison of their static constants obtained via nanoindentation tests. Furthermore, the dynamic elastic constant values of both the alloys are lower than their static elastic constant values. This is more likely related to the different response of the material to the different stimuli. Different strains at different strain rates or frequencies are associated with dynamic and static conditions of testing and/or applications. Additional variations can be understood via thermokinetics associated with the LPBF-AM technique and resultant microstructural details during fabrication of Ti6Al4V.

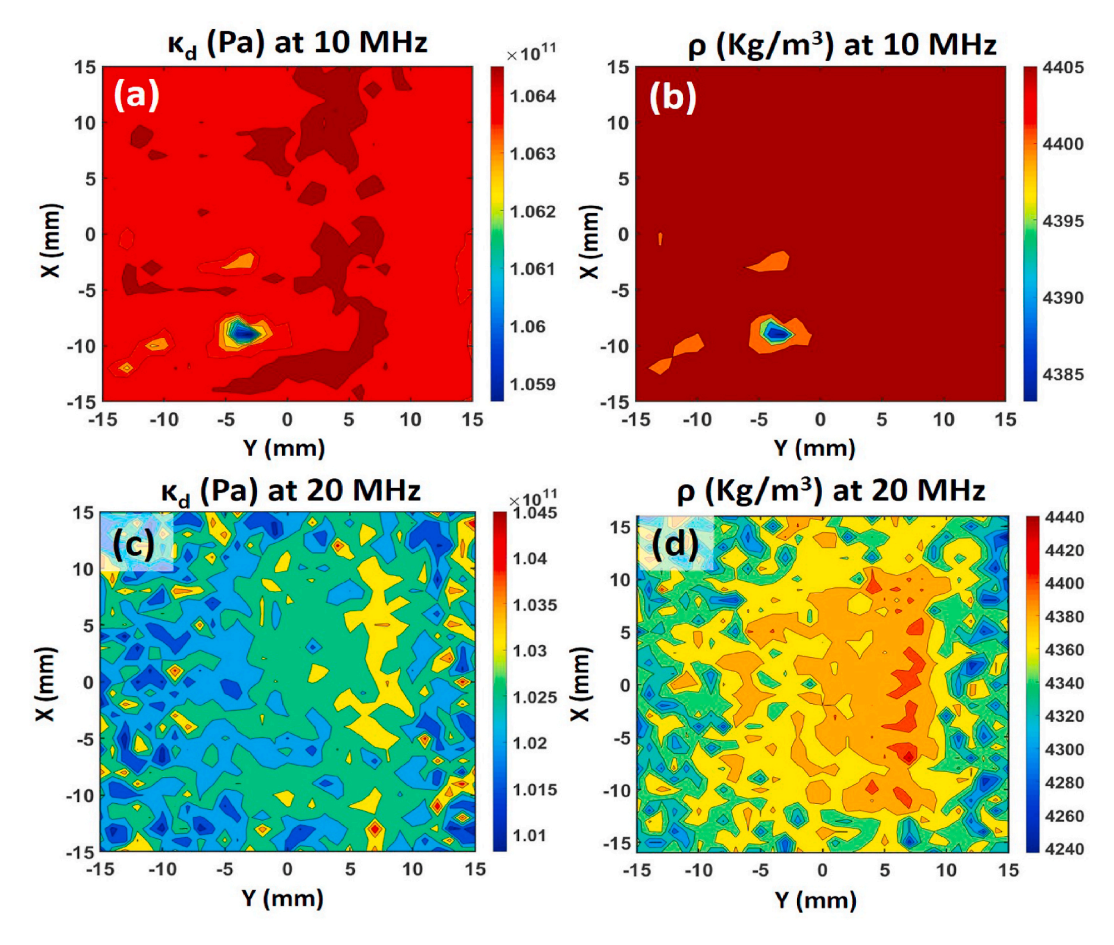


Fig. 3. The contour plots of effective dynamic bulk modulus and effective density of LPBF-AM Ti6Al4V at (a), (b) 10 MHz and (c), (d) 20 MHz.

Table 2Dynamic elastic constant and density of LPBF-AM and wrought Ti6Al4V.

Properties		LPBF-AM Ti6Al4V	Wrought Ti6Al4V
Dynamic You	ıng's Modulus (E _d /GPa)	123 ± 3.11	$138.06 {\pm} 0.25$
Dynamic Bul	k Modulus (K_d /GPa)	$102.2 {\pm} 2.1$	$110.5 {\pm} 0.8$
Dynamic She	ear Modulus (G_d /GPa)	$47.07{\pm}1.31$	$53.43 {\pm} 0.2$
Dynamic Poi	sson's Ratio (ν_d)	$0.3 {\pm} 0.003$	$0.28 {\pm} 0.0005$
Density (ρ/K	gm^{-3})	$4360 {\pm} 51$	4490±30

3.3. Comparison of elastic moduli

The static elastic moduli and hardness obtained by nanoindentation provides distinct variation in LPBF-AM Ti6Al4V, wrought Ti6Al4V, and WQ-Ti6Al4V. These variation were investigated through their individual microstructures. The optical microscopy observations of different regions of LPBF-AM Ti6Al4V indicated that the sample was free of any macro level physical defects (pore and cracks) (Fig. 4a). This also supports a comparable values of densities of LPBF-AM and wrought Ti6Al4V via pycnometer and EBME techniques (Tables 1 and 2). SEM micrographs of wrought Ti6AL4V primarily displayed α phase (area fraction- $0.9289\pm0.0022)$ with minor area fraction (0.07105 \pm 0.0023) of β phase (Fig. 4b). However, the microstructure did not reveal presence of any two dimensional crystallographic defect such as twins. On the contrary, SEM examination of LPBF-AM Ti6Al4V revealed the formation of hierarchical lath martensitic (α') structure (Fig. 4c). These nonequilibrium α' structures are formed within prior columnar β grains under the same set of processing parameters, as reported earlier by the authors [7,8,18]. Based on the computational model adapted from the earlier reported work of the authors [7], such a columnar morphology of prior β grains is formed under the influence of steep thermal gradients $(1.48\times10^6-1.58\times10^7~\text{K/m})$ mainly directed in the build-direction (Z) and the non-equilibrium $\alpha^{'}$ phase is formed under rapid cooling rates $(2.56\times10^7-4.82\times10^4~\text{K/s}).$ In addition, the martensitic laths possessed multiple internal twins throughout them (inset of Fig. 4c). The martensite laths were also seen in WQ-Ti6Al4V sample presented in Fig. 4d. However, these martensite were rarely twinned indicating formation of slipped martensite. The planer defects (twins) in LPBF-AM Ti6Al4V are evidence of generation and dissipation of extensive thermal stresses during LPBF-AM processing. This can be further realized by understanding the nature of thermo-mechanical cycles experienced during the LPBF-AM fabrication.

Based on the computational model described earlier, the components of the thermal stresses (σ_{xx} , σ_{yy} , and σ_{zz}) experienced by a given location, when the laser track runs over it, were predicted as presented in Fig. 5. The computational model-based predictions also indicated that for the volume of material at any location within the path of laser track, the thermal stresses are likely to substantially relax (dissipate) during melting and again start building up during solidification. However, a steep thermal gradient and associated maximum stress are generated only during solid-solid thermal transformation at a location within the solid region in the close proximity of and not within the laser track. Hence, a location experiencing solid-solid transition during a single heating-cooling cycle was considered. The thermal stresses in every direction (X, Y, and Z) result from uneven events of tensile and compressive thermal loads (expansion and contraction) (Fig. 5). In general, the stresses generated in the direction of laser movement (Y) are higher and peak at 720 MPa and compressive in nature. The rapidly alternatively generating tensile-compressive thermal stress events may

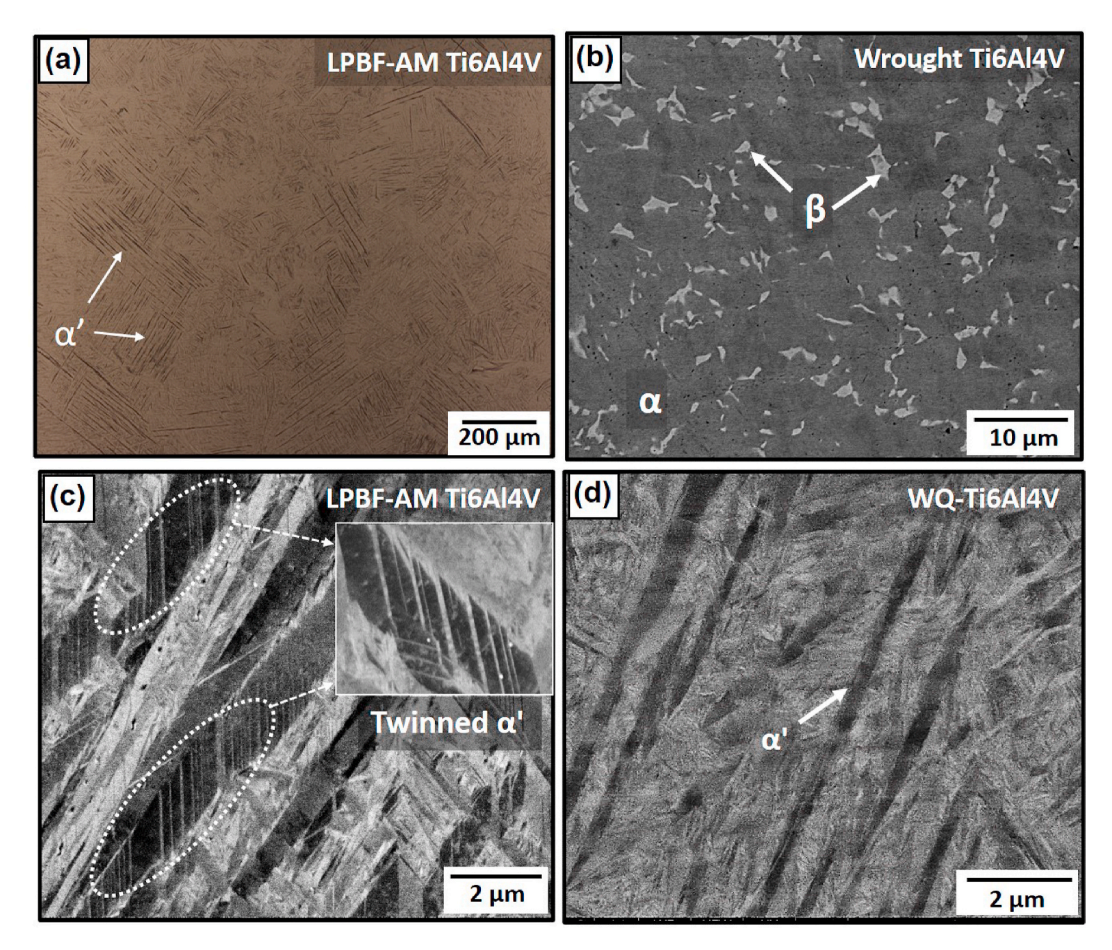


Fig. 4. (a) Low magnification optical overview showing the presence of α' martensite laths and absence of any physical defects, and SEM micrographs of (b) wrought Ti6Al4V, (c) LPBF-AM Ti6Al4V and (d) WQ-Ti6Al4V.

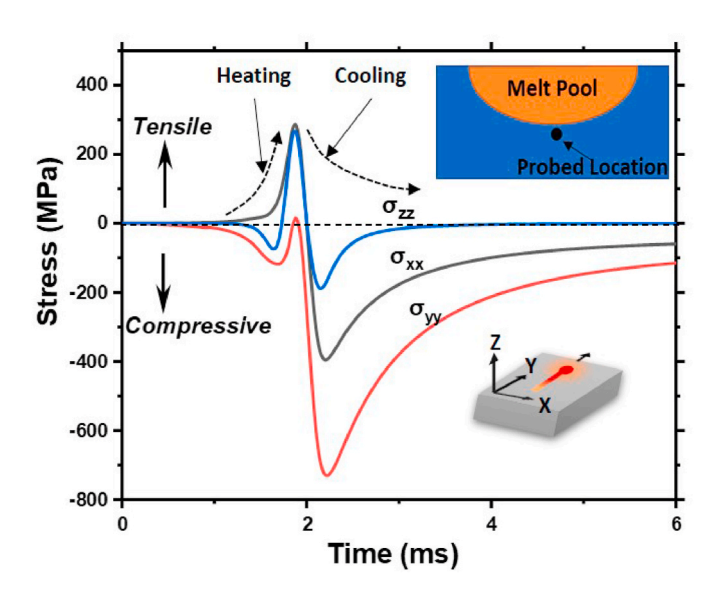


Fig. 5. Numerically predicted thermal stress components at a given location of LPBF-AM Ti6Al4V due to passage of single laser track.

constantly and simultaneously partially relax (dissipate) through multiple physical mechanisms (microstructural, phase, and crystallographic defects evolution). The extent of these mechanisms for dissipation of thermal stresses is likely to vary based on the combination of set of processing parameters and the type of processed material. Under such

high stresses, as predicted by the thermomechanical model, the lattice invariant shear during martensite transformation is highly likely to be accommodated by internal transformation twinning within martensite lath in LPBF-AM fabricated Ti6Al4V [19]. Furthermore, each heating-cooling cycle induces dynamic loading of tension and compression through uneven tensile and compressive thermal stresses which are accumulated with each laser track while building a multi-track layer and even further through the building of subsequent multiple layers during LPBF-AM fabrication. These accumulated thermal stresses are likely to be partially accommodated by crystallographic defects such twins and dislocations and partially remain as residual stress which elastically stretch or compress lattice. Thus, the intrinsic nature of the LPBF-AM process is likely to lead to high defect density and residual stresses. However, extremely high stresses are generally accommodated via the generation of crystallographic twins than dislocations, which can be transformation twins (generated during martensite formation) and deformation twins to accommodate additionally accumulated stresses with multiple thermal cycles, as observed in LPBF-AM Ti6Al4V (Fig. 4c). Although stresses generated during water quenching are also likely to be high, they are not comparable to the extreme thermal stresses generated during the LPBF-AM process. This is because the melt pool dimensions in LPBF-AM are microscopic (30-200 μm depth and 100-500 μm) and are quenched in the surrounding solid metal carrying low specific heat and high thermal conductivity. On the contrary, during water-quenching, even though the volume of a block of the sample (1 mm³) is small, it is quenched in water, which possesses relatively higher specific heat and lower thermal conductivity than metals. Thus, relatively lower cooling rates and, in turn, lower thermal stresses are generated in WQ-Ti6Al4V, and lattice invariant shear is

mainly primarily accommodated by dislocations via slip [19] and rarely via twinning (Fig. 4d). Furthermore, additionally accumulated stresses are also accommodated by the generation and evolution of dislocations. Consequently, it can be claimed that dislocation density is likely to be higher in WQ-Ti6Al4V than in LPBF-AM Ti6Al4V that possessed a predominance of twins than dislocations (Fig. 4c and d).

Every defect dislocation is associated with the distorted atomic lattice and local elastic strain gradient. This affects the local interatomic forces and spacing, which in turn is associated with the fundamental nature of the modulus of a given material. The presence of residual stresses responsible for elastically strained lattice is likely to affect the interatomic distance and force at a macro level, thereby affecting the elastic modulus. In addition, several studies focusing on the effects of work hardening have reported a decrease in the elastic constants with the increase in the degree of work hardening [20,21]. At the core of any dislocation, the interatomic spacing is comparatively larger, which weakens the forces of attraction among them, thereby reducing the elastic modulus locally. Thus, with a higher density of dislocations, and static and dynamic elastic constants of WQ-Ti6Al4V can be lower than wrought and LPBF-AM Ti6Al4V (Table 2). The presence of high-density dislocations obstructs the motion of dislocation during deformation, thereby strengthening the material. On the other hand, presence twin boundaries improve ductility while maintaining strength [22-24]. This is supported by the higher hardness exhibited by WQ-Ti6Al4V (4.34 \pm 0.05 GPa) than that of LPBF-AM Ti6Al4V (3.63 \pm 0.07 GPa) and wrought Ti6Al4V (3.84±0.17 GPa), which, in turn, support the likelihood of high dislocation density in WQ-Ti6Al4V and high twin density in LPBF-AM Ti6Al4V.

4. Conclusion

Dynamic characteristics of LPBF-AM Ti6Al4V evaluated using the EBME technique revealed lower values of dynamic elastic constants compared to that of wrought Ti6Al4V. The static elastic constants of LPBF-AM Ti6Al4V and wrought Ti6Al4V were higher than their dynamic elastic constant values. The static moduli comparison of the different alloys revaled that elastic moduli corresponding to LPBF-AM Ti6Al4V were relatively lower (22-26%) than the conventionally fabricated wrought Ti6Al4V and higher (18-21%) than that of WQ-Ti6Al4V sample. Microstructural analysis of LPBF-AM Ti6Al4V revealed a high density of internal twins within the laths of martensite, whereas martensite laths in WQ-Ti6Al4V sample were seldomly twinned. The rationale for high twin density in a non-equilibrium phase was realized through thermokinetics and thermomechanical coupled computational model. Numerically predicted thermal stresses during a single laser track of the LPBF-AM fabrication conducted by the parameters employed in the present work, rapidly varied in the range of 49-720 MPa thereby generating multiple crystallographic twins to dissipate the thermal stresses. The WQ-Ti6Al4V alloy exhibited highest hardness (4.34±0.05 GPa) and lowest elastic modulus compared to LPBF-AM Ti6Al4V and wrought Ti6Al4V.

CRediT authorship contribution statement

Mangesh V. Pantawane: Conceptualization, Methodology, Software, Formal analysis, Writing – original draft. Teng Yang: Data curation, Writing – original draft. Yuqi Jin: Data curation, Visualization. Sangram Mazumder: Data curation, Formal analysis. Mayur Pole: Data curation, Formal analysis. Sriswaroop Dasari: Data curation. Arkadii Krokhin: Writing – review & editing. Arup Neogi: Resources, Writing – review & editing. Narendra B. Dahotre: Resources, Writing – review & editing. Narendra B. Dahotre: Resources, Writing – review & editing, Supervision, Funding acquisition.

Declaration of competing interest

The authors declare that they have no known competing financial interests or personal relationships that could have appeared to influence the work reported in this paper.

Acknowledgment

The authors acknowledge the infrastructure and support of Center for Agile & Adaptive and Additive Manufacturing (CAAAM) funded through State of Texas Appropriation #190405-105-805008-220 and Materials Research Facility (MRF) at the University of North Texas. AN, AK, JY acknowledges the support of the National Science Foundation - Emerging Frontiers in Research and Innovation (EFRI) grant (#1741677).

References

- [1] Tuan D. Ngo, Alireza Kashani, Gabriele Imbalzano, Kate TQ. Nguyen, David Hui, Additive manufacturing (3d printing): a review of materials, methods, applications and challenges, Compos. B Eng. 143 (2018) 172–196.
- [2] Eyitayo Olatunde Olakanmi, R.F. Cochrane, K.W. Dalgarno, A review on selective laser sintering/melting (sls/slm) of aluminium alloy powders: processing, microstructure, and properties, Prog. Mater. Sci. 74 (2015) 401–477.
- [3] Dodd Bradley, Yilong Bai, Adiabatic Shear Localization: Frontiers and Advances, Elsevier, 2012.
- [4] Wit Grzesik, Advanced Machining Processes of Metallic Materials: Theory, Modelling and Applications, Elsevier, 2008.
- [5] Hans-Jakob Schindler, On quasi-non-destructive strength and toughness testing of elastic-plastic materials, Int. J. Solid Struct. 42 (2) (2005) 717–725.
- [6] William D. Callister, David G. Rethwisch, Materials Science and Engineering: an Introduction, Wiley, New York, 2018.
- [7] V Pantawane Mangesh, Yee-Hsien Ho, Sameehan S. Joshi, Narendra B Dahotre, Computational assessment of thermokinetics and associated microstructural evolution in laser powder bed fusion manufacturing of Ti6Al4V alloy, Sci. Rep. 10 (1) (2020) 1–14.
- [8] V Pantawane Mangesh, Sriswaroop Dasari, Mantri Srinivas Aditya, Rajarshi Banerjee, Narendra B Dahotre, Rapid thermokinetics driven nanoscale vanadium clustering within martensite laths in laser powder bed fused additively manufactured Ti6Al4V, Materials Research Letters 8 (10) (2020) 383–389.
- [9] J.-L. Gennisson, Thomas Deffieux, Mathias Fink, Michaël Tanter, Ultrasound elastography: principles and techniques, Diagnostic and interventional imaging 94 (5) (2013) 487–495.
- [10] Yuqi Jin, Ezekiel Walker, Arkadii Krokhin, Hyeonu Heo, Tae-Youl Choi, Arup Neogi, Enhanced instantaneous elastography in tissues and hard materials using bulk modulus and density determined without externally applied material deformation, IEEE Trans. Ultrason. Ferroelectrics Freq. Contr. (2019).
- [11] Yuqi Jin, Ezekiel Walker, Hyeonu Heo, Arkadii Krokhin, Tae-Youl Choi, Arup Neogi, Nondestructive ultrasonic evaluation of fused deposition modeling based additively manufactured 3d-printed structures, Smart Mater. Struct. 29 (4) (2020), 045020.
- [12] T. Ahmed, H.J. Rack, Phase transformations during cooling in $\alpha+\beta$ titanium alloys, Mater. Sci. Eng., A 243 (1–2) (1998) 206–211.
- [13] L. Parry, I.A. Ashcroft, D Wildman Ricky, Understanding the effect of laser scan strategy on residual stress in selective laser melting through thermo-mechanical simulation, Additive Manufacturing 12 (2016) 1–15.
- [14] Zhongxue Feng, Yingxiang Yang, Zhichao Xu, Qingnan Shi, Effect of martensitic transformation on elastic modulus anisotropy of ti-6al-4v alloy, Mater. Res. 21 (4) (2018).
- [15] Gerhard Welsch, Rodney Boyer, E.W. Collings, Materials Properties Handbook: Titanium Alloys, ASM international, 1993.
- [16] Y Morris Wang, Thomas Voisin, Joseph T. McKeown, Jianchao Ye, Nicholas P. Calta, Zan Li, Zhi Zeng, Yin Zhang, Wen Chen, Tien Tran Roehling, et al., Additively manufactured hierarchical stainless steels with high strength and ductility, Nat. Mater. 17 (1) (2018) 63–71.
- [17] Wen Chen, Thomas Voisin, Yin Zhang, Jean-Baptiste Florien, Christopher M. Spadaccini, David L. McDowell, Ting Zhu, Y Morris Wang, Microscale residual stresses in additively manufactured stainless steel, Nat. Commun. 10 (1) (2019) 1–12
- [18] V Pantawane Mangesh, Teng Yang, Yuqi Jin, Sameehan S. Joshi, Sriswaroop Dasari, Abhishek Sharma, Arkadii Krokhin, Srivilliputhur G. Srinivasan, Rajarshi Banerjee, Arup Neogi, Narendra B Dahotre, Crystallographic texture dependent bulk anisotropic elastic response of additively manufactured Ti6Al4V, Sci. Rep. 11 (633) (2021) 1–10.
- [19] C.M. Wayman, The phenomenological theory of martensite crystallography: Interrelationships, Metall. Mater. Trans. 25 (9) (1994) 1787–1795.
- [20] Antoni Roca, Aránzazu Villuendas, Ignacio Mejía, Josep Antonio Benito, Núria Llorca-Isern, Jordi Llumà, Jordi Jorba, Can young's modulus of metallic alloys change with plastic deformation?, in: Materials Science Forum, vol. 783 Trans Tech Publ, 2014, pp. 2382–2387.

- [21] Qingda Li, Guomin Hua, Hao Lu, Bin Yu, D.Y. Li, Understanding the effect of plastic deformation on elastic modulus of metals based on a percolation model with electron work function, J. Occup. Med. 70 (7) (2018) 1130–1135.
- [22] J. Wang, L. Liu, C.N. Tomé, S.X. Mao, S.K. Gong, Twinning and de-twinning via glide and climb of twinning dislocations along serrated coherent twin boundaries in hexagonal-close-packed metals, Materials Research Letters 1 (2) (2013) 81–88.
- [23] M.H. Yoo, J.R. Morris, K.M. Ho, S.R. Agnew, Nonbasal deformation modes of hcp metals and alloys: role of dislocation source and mobility, Metall. Mater. Trans. 33 (3) (2002) 813–822.
- [24] Jian Wang, J.P. Hirth, C.N. Tomé, (1 012) twinning nucleation mechanisms in hexagonal-close-packed crystals, Acta Mater. 57 (18) (2009) 5521–5530.